

Received: 13 January 2016 Accepted: 21 June 2016 Published: 13 July 2016

# **OPEN** Comprehensive design of omnidirectional high-performance perovskite solar cells

Yutao Zhanq<sup>1,\*</sup> & Yimin Xuan<sup>1,2,\*</sup>

The comprehensive design approach is established with coupled optical-electrical simulation for perovskite-based solar cell, which emerged as one of the most promising competitors to silicon solar cell for its low-cost fabrication and high PCE. The selection of structured surface, effect of geometry parameters, incident angle-dependence and polarization-sensitivity are considered in the simulation. The optical modeling is performed via the finite-difference time-domain method whilst the electrical properties are obtained by solving the coupled nonlinear equations of Poisson, continuity, and driftdiffusion equations. The optical and electrical performances of five different structured surfaces are compared to select a best structured surface for perovskite solar cell. The effects of the geometry parameters on the optical and electrical properties of the perovskite cell are analyzed. The results indicate that the light harvesting is obviously enhanced by the structured surface. The electrical performance can be remarkably improved due to the enhanced light harvesting of the designed best structured surface. The angle-dependence for s- and p-polarizations is investigated. The structured surface exhibits omnidirectional behavior and favorable polarization-insensitive feature within a wide incident angle range. Such a comprehensive design approach can highlight the potential of perovskite cell for power conversion in the full daylight.

With the rapid consumption of fossil fuels like coal, oil and natural gas, it is urgent to develop alternative approach to supply sustainable energy production with the growing global energy demand<sup>1</sup>. Solar energy is one of the most potential abundant, clean and renewable energy resources to resolve the energy crisis<sup>2</sup>. Photovoltaic solar cell has been a more and more effective approach to utilize the solar energy. Plenty of efforts have been devoted to the investigation of the solar cell to increase the power conversion efficiency (PCE) and reduce the cost of the solar cell<sup>3-6</sup>. Solid-state organo-metal halide perovskite solar cells emerged as a kind of promising alternative to the existing photovoltaic technologies<sup>7</sup>. The solid-state perovskite solar cells are derived from the liquid-state dye-sensitized solar cells<sup>8</sup>. Recently, the energy conversion efficiency of the solid-state perovskite solar cells has quickly surpassed that of the conventional dye-sensitized solar cells and attracted more and more attentions9.

Perovskite refers to the crystal structure of the mineral family of ABX<sub>3</sub>, where A is the monovalent or divalent metal and B is the tetravalent or divalent metal. X is the chalcogen or halogen<sup>10</sup>. There are hundreds of materials adopt to this crystal structure, such as CsPbCl<sub>3</sub>, BaTiO<sub>3</sub>, (NH4)SnI<sub>3</sub>, and CH<sub>3</sub>NH<sub>3</sub>PbI<sub>3</sub><sup>11-13</sup>. Because of the excellent solar-to-electricity energy conversion performance of CH<sub>3</sub>NH<sub>3</sub>PbI<sub>3</sub> material, it is applied to the photovoltaic cell and has attracted great attentions. For a long time, CH<sub>3</sub>NH<sub>3</sub>PbI<sub>3</sub> was implemented as sensitizer particles in dye-sensitized solar cells (DSSC) with liquid-electrolyte<sup>14</sup>. The function of the electrolyte is to regenerate the oxidized dye and to transport the holes to the external circuit. As a result of the concerns over solvent leakage and corrosion, recent attentions have been focused on replacing this electrolyte with solid-state hole transporter alternatives to create fully solid-state electronic DSSCs<sup>15</sup>. Bach et al. developed the perovskite cell by replacing the liquid-electrolyte with solid-state hole-transport material (HTM) 2,2',7,7' tetrakis (N,N-di-p-methoxyphenyl-amine) 9,9' -spirobifluorene (OMeTAD) and the cell performance is obviously improved16. In 2012, a strong efficiency improvement to 9% was achieved by Kim et al. by replacing the liquid-electrolyte with solid HTM17. However, the energy conversion efficiency is still very low, even lower than that of original electrochemical cell. In order to increase the conversion efficiency, great efforts have been devoted

<sup>1</sup>School of Energy and Power Engineering, Nanjing University of Science & Technology, Nanjing 210094, China. <sup>2</sup>School of Energy and Power Engineering, Nanjing University of Aeronautics & Astronautics, Nanjing 210094, China. \*These authors contributed equally to this work. Correspondence and requests for materials should be addressed to Y.X. (email: ymxuan@mail.njust.edu.cn)

to the investigations of the optical and electrical characteristics of solid-state perovskite solar cell. Lee et al. replaced the mesoporous n-type  $TiO_2$  with insulating  $Al_2O_3$  scaffold and found that the great increase in  $V_{oc}$  is observed and a PCE of 10.9% is achieved<sup>18</sup>. Kim et al. reported a highly efficient solar cell based on a submicrometer rutile TiO<sub>2</sub> nanorod sensitized with CH<sub>3</sub>NH<sub>3</sub>PbI<sub>3</sub> nanodots<sup>19</sup>. It was found that the short-circuit photocurrent density of  $15.6 \,\mathrm{mA/cm^2}$ , open-circuit voltage  $(V_{\mathrm{oc}})$  of 955 mV and fill factor (FF) of 0.63, which lead to a PCE of 9.4%, are realized by such a perovskite solar cell. Concurrently, the development in the understanding of operation mechanism confirming long distance charge transport has supported the utilization of conventional thin film architectures, which simplifies the fabrication of solution-based perovskite solar cell at low temperature<sup>20–22</sup>. According to the Snaith's investigation, the intrinsic CH<sub>3</sub>NH<sub>3</sub>PbI<sub>3</sub> layer was sandwiched by the p-type HTM and n-type TiO<sub>2</sub> layer. Consequently the whole structure appears as p-i-n architecture<sup>23</sup>. The energy conversion efficiency was greatly increased by the improvements in the material processing and solar cell fabrication. Liu and Kelly used a thin film of ZnO particles as electron-transport material in CH<sub>3</sub>NH<sub>3</sub>PbI<sub>3</sub> based solar cells. The PCE was as high as 15.7% and the processing temperature was greatly reduced<sup>24</sup>. Zhou et al. remarkably suppressed the carrier recombination in the absorber, facilitated carrier injection into the carrier transport layers, and maintained good carrier extraction at the electrodes by controlling the formation of the perovskite layer and careful choices of other materials<sup>25</sup>. The energy conversion efficiency was observed to be boosted to 16.6% on average with the highest efficiency of 19.3% in a planar geometry without antireflective coating. With an unprecedented short development period of perovskite solar cells, the PCE has reached over 20%<sup>26</sup>.

The prior investigation of the perovskite solar cell was prominently performed by the experimental methods and the electrical property is merely considered. Recently, several groups have reported their theoretical research about perovskite solar cell performance, including optical and electrical features. Liu  $et\ al.$  simulated the planar heterojunction-based perovskite solar cells with AMPS-1D<sup>27</sup>. The simulation results revealed a great dependence of energy conversion efficiency on the thickness and defect density of the perovskite layer. The energy conversion efficiency over 20% was obtained. However, the optical properties were not included in their research and the incident solar energy was assumed to be completely absorbed. Ball  $et\ al.$  used an optical model of perovskite planar heterojunction solar cells which has been optimized by the transfer-matrix formalism using experimentally determined complex refractive index to analysis the optical and electrical cell performances<sup>28</sup>. The simulated and experimental results coincided well with each other. The short-circuit current ( $J_{sc}$ ) density of 22.6 mA/cm<sup>2</sup> is obtained under AM1.5 sunlight with 104.7 mW/cm<sup>2</sup> irradiance. Yet up to now, there is little investigation concerning the effect of micro-structure on the optical and electrical performances of perovskite solar cells.

Due to the changing incident angle of sunlight, the auto-solar tracker is generally employed to follow the sun. However, the complicated auto-solar tracker is expensive and delicate as a result of the existence of moving components. Hence it is necessary and more attractive to investigate the omnidirectional structured surfaces to achieve light trapping in solar cells. For example, the reflection is suppressed by sub-wavelength Mie resonators within a broad wavelength band and wide incident angles<sup>29</sup>. Moth-eye structure has been proved to possess excellent broadband omnidirectional optical features. Song et al. have proved that the moth-eye structure could be used to realize the omnidirectional light trapping in GaAs solar cells<sup>30</sup>. Tommila et al. fabricated the SiN<sub>x</sub> coated moth-eye coating by nanoimprint lithography directly on dilute nitride solar cell<sup>31</sup>. The mean reflection within the spectral range of 320-1800 nm remained under 5% for incident angles up to 45° and the clear increase of electrical performance was verified. Yamada et al. characterized the antireflection moth-eye films placed on top of crystalline silicon photovoltaic modules by indoor and outdoor experiments in conversion efficiency<sup>32</sup>. According to their investigations, it is found that the use of antireflection moth-eye films offers the best advantages. With the large aspect ratio of the height to the width, the surface possessed angle-independent spectral feature<sup>33</sup>. In addition, the sunlight is the natural light, which includes all polarization states. The light-trapping is remarkably influenced by the polarization of the incident light at oblique incidence. Therefore, the structured surface of the perovskite cell is expected to possess high absorption for all polarizations.

Yet up to now, the investigation of perovskite solar cell is mainly focused on the experimental research and the film stack is the mainstream structured surface, in which the performance of the perovskite solar cell is generally dependent on the incident angle. The systematical design method for the optical-electrical properties of the perovskite solar cell is scarcely developed. The absorption of the cell is not high enough and the micro-structured surface to enhance the light harvesting is little considered. The incident angle-dependence and polarization-sensitivity are hardly involved.

This paper describes a comprehensive design approach with optical-electrical simulation for perovskite solar cells. The selection of structured surface, effects of geometry parameters, incident angle-dependence and polarization-sensitivity are involved in the simulation. The optical absorption is calculated by the finite-difference time-domain (FDTD) method and the electrical performance is obtained by solving the coupled nonlinear equations of Poisson, continuity, and drift-diffusion equations. Experimental results in the literature are used to validate the theoretical model and the parameters employed in the simulations. The optical absorption and electrical properties of five different structured surfaces are calculated and compared to select a best structured surface with the highest PCE for perovskite cell. The effects of the geometry parameters on the optical response and electrical properties of the structured surface are analyzed. The incident angle-dependence for s- and p-polarizations is investigated.

#### Results

**Theoretical model validation.** The perovskite cell is generally consisted of SiO<sub>2</sub>, FTO, TiO<sub>2</sub>, CH<sub>3</sub>NH<sub>3</sub>PbI<sub>3</sub> and HTM. FTO is the cathode and Ag is the anode. TiO<sub>2</sub> and HTM respectively serve as electron transport material and hole transport material. CH<sub>3</sub>NH<sub>3</sub>PbI<sub>3</sub> film is the intrinsic photoactive layer. The spiro-OMeTAD is applied as the HTM. The optical constants of SiO<sub>2</sub>, FTO, TiO<sub>2</sub>, CH<sub>3</sub>NH<sub>3</sub>PbI<sub>3</sub> and HTM used in this paper are obtained from Ball's investigation, which are measured by the spectroscopic ellipsometry<sup>34</sup>, and the optical

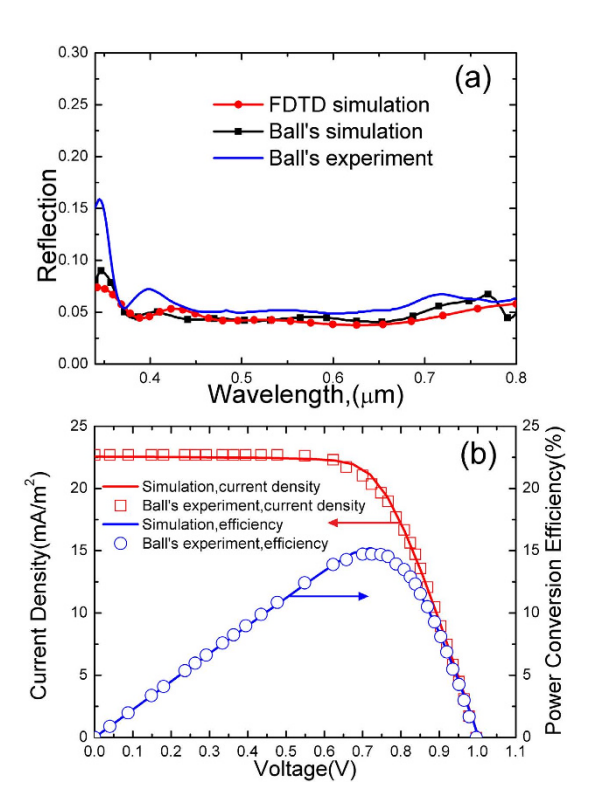


**Figure 1. Validation of theoretical model. (a)** Comparison of the simulated optical properties of planar film structure with the experimental data<sup>28</sup>. **(b)** Comparison of the simulated electrical performances of planar film structure with the experimental data<sup>28</sup>.

constant of Ag is selected from ref. 35. The electrical properties of the materials utilized in perovskite solar cell are listed in Supplementary Table S1. The Shockley-Read-Hall (SRH) recombination and surface recombination are considered in the simulation.

The theoretical model is validated against the investigation reported by Ball  $et~al.^{28}$ . The spectral features of the structured surface in ref. 28 and the optical generation are calculated by FDTD method. With this optical generation, the current-voltage characteristics are obtained by solving three basic semiconductor equations (see the Methods section for more details). As shown in Fig. 1a, the simulated optical results are compared with the numerical and experimental data from Ball  $et~al.^{28}$ . The reflection is about 0.05, which is comparable to that of the AR-coated Si solar cells<sup>36,37</sup>. The calculated results coincide well with the theoretical and experimental data from Ball et~al. The slight deviation between the simulated results and the Ball's theoretical data, which are obtained by the transfer matrix method, is attributed to the difference between the calculation methods. The simulated electrical characteristics are compared with the experimental data from Ball et~al. in Fig. 1b. The  $J_{\rm sc}$  of 22.6 mA/cm² and  $V_{\rm oc}$  of 1 V are realized. It is found that the numerical results and experimental data are in good agreement across the voltage range from zero to the  $V_{\rm oc}$  (0–1 V). This implies that the optical and electrical parameters applied here are reasonable. The theoretical method and the established model are valid and applicable.

**Selection of structured surface for perovskite solar cell.** In order to select a best structured surface for perovskite solar cell, five possible structured surface, including film stack, structured surface with CH<sub>3</sub>NH<sub>3</sub>PbI<sub>3</sub> grating, structured surface with TiO2 grating, structured surface with SiO2 grating and structured surface with TiO<sub>2</sub> grating and SiO<sub>2</sub> grating, are considered to enhance light harvesting and PCE herein, as shown in Fig. 2a-e. For convenience, the five structured surfaces are referred to simply as structured surface A, B, C, D and E in order, respectively. The film stack structure in Fig. 2a is the simplest and the most investigated structure of perovskite solar cell. Therefore, the performance of structured surface A is treated as the reference to other structured surfaces. The structured surface is periodically arranged and  $\Lambda$  is the period of structured surface.  $r = \Lambda/2$  is the bottom radius of the SiO<sub>2</sub> moth-eye grating.  $h_1$  is the thickness of Ag film and  $h_2$  is the thickness of HTM film.  $h_3$  is the thickness of CH<sub>3</sub>NH<sub>3</sub>PbI<sub>3</sub> structure.  $h_4$  is the thickness of TiO<sub>2</sub> film and  $h_5$  is the thickness of FTO film.  $h_6$  is the thickness of the SiO<sub>2</sub> substrate and  $h_7$  is the height of the Si moth-eye structure.  $h_8$  is the height of the  $\text{TiO}_2$  grating.  $h_9$  is the height of the  $\text{CH}_3\text{NH}_3\text{PbI}_3$  grating.  $f_1$  is the filling ratio of  $\text{TiO}_2$  grating.  $f_2$  is the filling ratio of CH<sub>3</sub>NH<sub>3</sub>PbI<sub>3</sub> grating. These two filling ratios are always set to 0.5 and 0.45, respectively. The period of  $CH_3NH_3PbI_3$  grating is set to equal to the period of moth-eye structure.  $\theta$  is the incident angle. The black dash line indicates the normal direction of the top interface. This paper focuses on the theoretical comprehensive design method of perovskite solar cells and the experiment is not considered. The existing literatures can verify the feasibility of the fabrications of designed structured surfaces. The FTO grating nanostructure is patterned first and

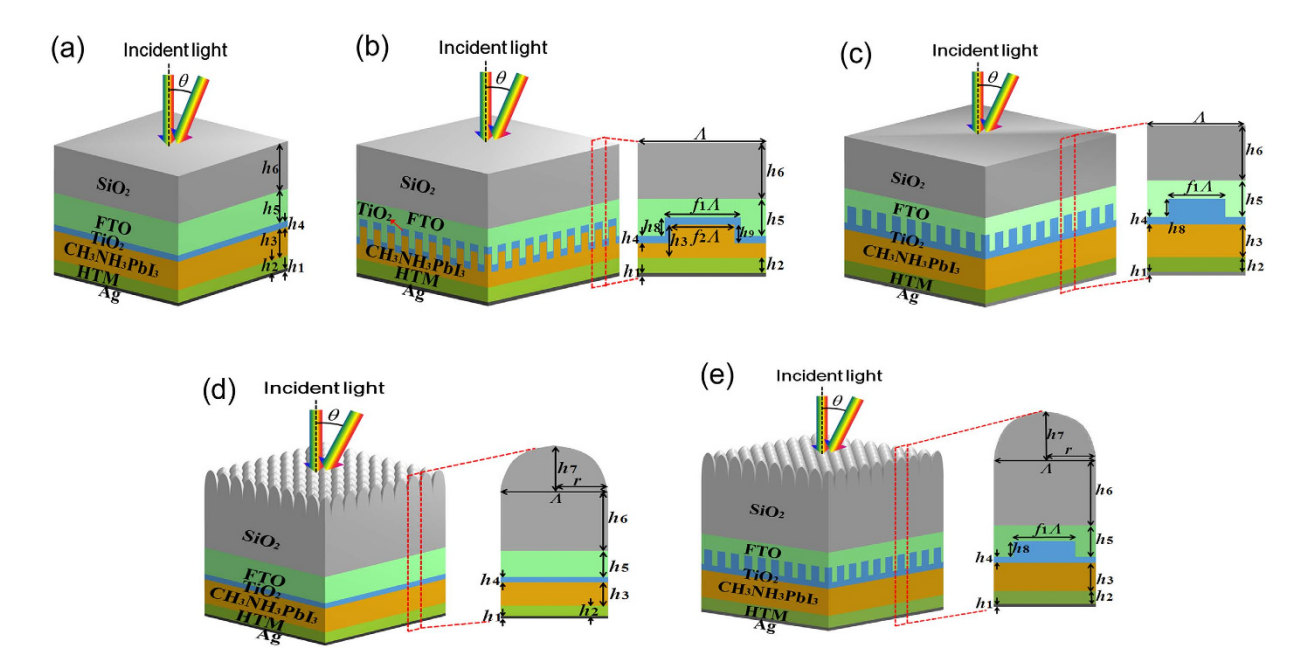


Figure 2. Device architectures and geometry parameter indications of five different structured surfaces. (a) Structured surface A: film stack. (b) Structured surface B: structured surface with CH<sub>3</sub>NH<sub>3</sub>PbI<sub>3</sub> grating. (c) Structured surface C: structured surface with TiO<sub>2</sub> grating. (d) Structured surface D: structured surface with SiO<sub>2</sub> grating. (d) Structured surface D: structured surface with TiO<sub>2</sub> grating and SiO<sub>2</sub> grating. The black dash line indicates the normal direction of the top interface.

Structure	$h_1(\mu m)$	h <sub>2</sub> (μm)	h <sub>3</sub> (μm)	h <sub>4</sub> (μm)	h <sub>5</sub> (μm)	$h_6(\mu m)$	$h_7(\mu m)$	h <sub>8</sub> (μm)	h <sub>9</sub> (μm)
Structured surface A	0.01	0.35	0.75	0.05	1	20	_	_	_
Structured surface B	0.01	0.35	0.75	0.05	1	20	_	0.4	0.4
Structured surface C	0.01	0.35	0.75	0.05	1	20	_	0.4	_
Structured surface D	0.01	0.35	0.75	0.05	1	20	6	_	_
Structured surface E	0.01	0.35	0.75	0.05	1	20	6	0.4	_

Table 1. Geometry parameters of five structured surfaces of perovskite solar cells.

the other layers or nanostructures are grown one by one. The  $SiO_2$  moth-eye grating is patterned on the bottom of  $SiO_2$  substrate at last. The detail fabrication methods can be found in many published literatures<sup>38,39</sup>.

Since the scattering is strongest when the structural size is comparable to the incident wavelength and the center wavelength of the solar spectrum is around 0.6 µm, the optical absorption of the structured surface with the period of 0.6 µm is highest (Supplementary Fig. S1). Thus the period of the structured surface discussed in this paper is always set to 0.6 µm. The geometry parameters of five structured surfaces are listed in Table 1. The optical absorption and JV-charateristics of different structured surfaces are calculated and the results are compared in Fig. 3. The optical absorption is obviously enhanced by the structured surface, as shown in Fig. 3a. The overall absorption means the absorption of the whole structured surface. It can be found that the structured surface E and structured surface D possess the overall absorption significantly higher than that of the structured surface A due to the influence of SiO<sub>2</sub> grating. The SiO<sub>2</sub> grating on one hand provides a smoother gradient effective refractive index; on the other hand, the SiO<sub>2</sub> grating induces scattering, which further suppresses the reflection. Therefore, the reflection at the SiO<sub>2</sub>/air interface is obviously suppressed and the absorption is enhanced. Simultaneously, it can be observed that the overall absorption of the structured surface E is highest among five structured surfaces due to the double scatterings of the SiO<sub>2</sub> grating and TiO<sub>2</sub> grating. The light entering the solar cell is further scattered by the TiO<sub>2</sub> grating and the absorption is enhanced. For perovskite solar cell, the absorption of intrinsic CH<sub>3</sub>NH<sub>3</sub>PbI<sub>3</sub> layer is vital because only the photons absorbed by the intrinsic layer can be converted into electricity power. Hence it is of great interest to investigate the intrinsic absorption of the cell. As shown in Fig. 3b, the intrinsic absorption of five structured surfaces is compared to choose a best structured surface with highest intrinsic absorption. It is seen that the intrinsic absorption of structured surface B is remarkably higher than that of other structured surfaces. This is attributed to that the CH<sub>3</sub>NH<sub>3</sub>PbI<sub>3</sub> grating scatters the light and more photons are absorbed by the CH<sub>3</sub>NH<sub>3</sub>PbI<sub>3</sub> layer. The intrinsic absorption of the structured surface E is lower than that of the structured surface B while it is higher than that of the rest three structured surfaces. This is mainly resulted from the double scatterings. Figure 3c,d illustrate the average overall absorption and average intrinsic absorption of five structured surfaces. It can be found that the average overall absorption of structured surface E, which is as high as 0.971, is highest among five structured surfaces. The average overall absorption of

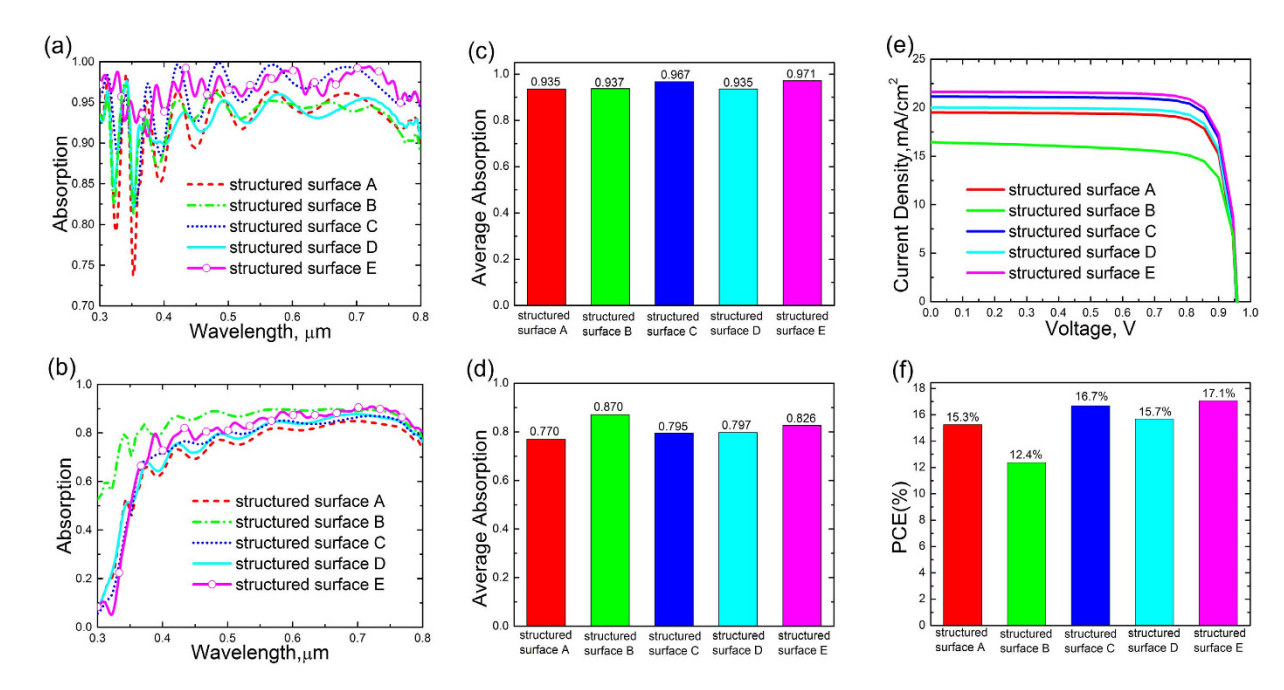


Figure 3. Spectral absorption and electrical properties of five different structured surfaces of perovskite solar cells . (a) Overall absorption of five different structured surfaces. (b) Intrinsic absorption of five different structured surfaces. (c) Average overall absorption of five different structured surfaces. (d) Average intrinsic absorption of five different structured surfaces. (e) JV-characteristics of five different structured surfaces. (f) Power conversion efficiencies of five different structured surfaces.

the planar film structure is lowest. The average intrinsic absorption of the structured surface B reaching as high as 0.870 is highest among five structured surfaces because of the scattering of the CH<sub>3</sub>NH<sub>3</sub>PbI<sub>3</sub> grating. In addition, although the average intrinsic absorption of the structured surface E is not as high as that of the structured surface B, it still reaches 0.826, which is obviously higher than that of structured surface A. This demonstrates that the absorption of perovskite solar cell can be effectively enhanced by the structured surfaces. For a solar cell, the electrical performance is vitally important and the high PCE is the ultimate destination. The JV-characteristics of five structured surfaces are illustrated in Fig. 3e. It is found that the structured surface E possesses the greatest  $I_{se2}$ which reaches as high as 21.64 mA/cm<sup>2</sup>, due to the enhanced intrinsic absorption. The J<sub>sc</sub> of the structured surface C is also obviously higher than that of structured surface A and is slightly smaller than that of the structured surface E. This demonstrates that the TiO<sub>2</sub> material is beneficial for the electron extraction and transport and it is suitable for the electron transport material. Despite of most significant intrinsic absorption among five different structured surfaces, the  $J_{sc}$  of the structured surface B is remarkably reduced to 16.43 mA/cm<sup>2</sup>. This is attributed to that the surface recombination velocity at CH<sub>3</sub>NH<sub>3</sub>PbI<sub>3</sub>/TiO<sub>2</sub> interface is significant and the CH<sub>3</sub>NH<sub>3</sub>PbI<sub>3</sub> grating increases the surface area so that the overall surface recombination is increased. Based on the JV-characteristics in Fig. 3e, the PCEs of five different structured surfaces for perovskite solar cell are obtained and shown in Fig. 3f. The structured surface E has the highest PCE of 17.1%, which is 1.8% higher than the PCE of 15.3% of structured surface A. The PCE of the structured surface B is as low as 12.4% due to the great surface recombination. Thus the structured surface E is the best structured surface among five structured surfaces because of its advanced light-harvesting and solar-to-electricity performances. In the following sections, the discussion is centered on the structured surface E. The height of CH<sub>3</sub>NH<sub>3</sub>PbI<sub>3</sub> grating h<sub>9</sub> is set to zero. The rest sizes of the structured surface E maintain the same as listed in Table 1.

Effect of the SiO<sub>2</sub> grating height  $h_7$ . For a solar cell employing the moth-eye antireflection structure, the gradient of effective refractive index is reduced so that the reflection is greatly suppressed and the absorption is enhanced with the increase of moth-eye grating height. As the moth-eye grating height is increased furthermore, the absorption tends to a saturation value (Supplementary Fig. S2). Consequently, the electrical properties of the structured surface are also influenced by the height of moth-eye grating. The  $J_{\rm sc}$ ,  $V_{\rm oc}$ , FF and PCE are four important parameters to evaluate the electrical performance of the solar cell. The effects of the SiO<sub>2</sub> grating height on these four parameters are shown in Fig. 4. The SiO<sub>2</sub> grating height of structured surface E is increased from  $0\,\mu$ m to  $8\,\mu$ m by the step of  $1\,\mu$ m. It is seen that the  $J_{\rm sc}$  is greatly increased as the SiO<sub>2</sub> grating height is increased from  $0\,\mu$ m to  $6\,\mu$ m. When the SiO<sub>2</sub> grating height is increased furthermore, the increase of  $J_{\rm sc}$  is very limited and  $J_{\rm sc}$  tends to a saturation current of  $21.78\,\text{mA/cm}^2$ . The  $J_{\rm sc}$  is mainly influenced by the intrinsic absorption. Thus the change of  $J_{\rm sc}$  with the increase of SiO<sub>2</sub> grating height coincides with the change of intrinsic absorption (Supplementary Fig. S2).  $V_{\rm oc}$  is almost constant around  $0.96\,\text{V}$ . This is lower than normal experimental value of  $1\,\text{V}$  due to significant SRH recombination caused by that the thickness of CH<sub>3</sub>NH<sub>3</sub>PbI<sub>3</sub> layer is larger than that in the normal experiment. FF is almost around 0.82. The PCE becomes higher as the SiO<sub>2</sub> grating height is increased

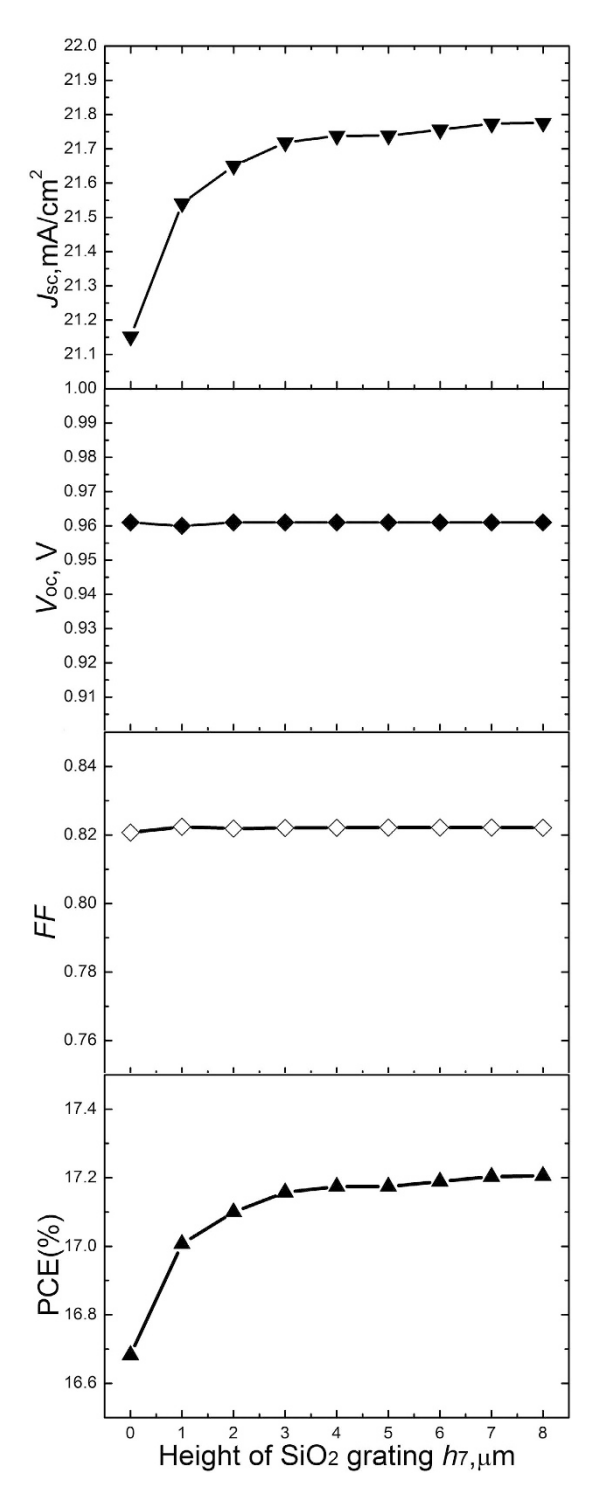


Figure 4. Effect of the  $SiO_2$  grating height on the electrical properties of structured surface E. The short-circuit currents, open-circuit voltages, fill factors and power conversion efficiencies under AM1.5 one sun illumination of the structured surfaces with different  $SiO_2$  grating heights are respectively depicted in four illustrations.

and finally reaches a saturation value about 17.2%. It has been well known that the PCE of solar cell can be expressed as PCE =  $P_{\rm max}/(100\,{\rm mA} \cdot {\rm V}) = (J_{\rm sc}V_{\rm oc}FF)/(100\,{\rm mA} \cdot {\rm V})$ , where  $P_{\rm max}$  is the maximum output power<sup>40</sup>. The  $V_{\rm oc}$  and FF are almost constants. The PCE is mainly influenced by  $J_{\rm sc}$ . Therefore, the change of PCE with the increase of SiO<sub>2</sub> grating height is the same as that of  $J_{\rm sc}$ . When the SiO<sub>2</sub> grating height equals 6  $\mu$ m, the PCE has nearly reaches the saturation value. Thus the SiO<sub>2</sub> grating height of 6  $\mu$ m is high enough to improve the performance of perovskite cell and this height is employed in the following sections.

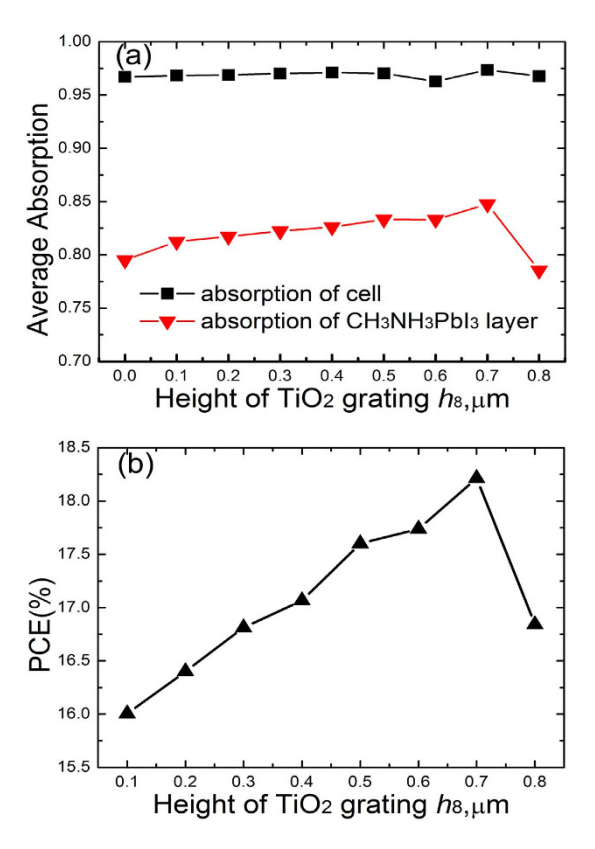


Figure 5. Effect of the  $TiO_2$  grating height on the optical and electrical performances of the structured surface E. (a) The average overall absorption and average intrinsic absorption of the structured surface E with different  $TiO_2$  grating heights. (b) The power conversion efficiencies of the structured surface E with different  $TiO_2$  grating heights.

**Effect of the TiO**<sub>2</sub> **grating height**  $h_8$ . Figure 5a shows the effect of the TiO<sub>2</sub> grating height on the optical performance of structured surface. The FDTD calculated results are integrated with AM 1.5 solar spectrum to acquire the average absorption. It can be seen that the average overall absorption almost keeps constant around 0.97 with the increase of TiO<sub>2</sub> grating height. The average intrinsic absorption is increased at the beginning with the increase of the  $TiO_2$  grating height. When the  $TiO_2$  grating height is increased to  $0.7 \,\mu m$ , the average intrinsic absorption reaches the maximum of 0.848 and then is reduced as the TiO<sub>2</sub> grating height is increased furthermore. Figure 5b shows the effect of TiO2 grating height on the PCE of the structured surface E. The PCE is also increased at the beginning with the increase of TiO2 grating height. When the TiO2 grating height is increased to 0.7 μm, the highest PCE of 18.2% is realized. With the further increase of TiO<sub>2</sub> grating height, the PCE is reduced. This is attributed to that the intrinsic absorption directly influences the  $J_{sc}$  of the structured surface. The  $J_{\rm sc}$  is increased from 20.35 mA/cm<sup>2</sup> to 22.98 mA/cm<sup>2</sup> when the TiO<sub>2</sub> grating height is increased from 0.1  $\mu$ m to  $0.7 \,\mu\text{m}$ . As the TiO<sub>2</sub> grating height is increased from  $0.7 \,\mu\text{m}$  to  $0.8 \,\mu\text{m}$ , the  $J_{\text{sc}}$  is reduced from  $22.98 \,\text{mA/cm}^2$  to 21.31 mA/cm<sup>2</sup>. This is mainly resulted from that the average intrinsic absorption of structured surface is reduced to 0.848 to 0.785, which leads to the decrease of photon-induced carriers. The  $V_{\rm oc}$  and the FF are almost constants (Supplementary Fig. S3). Therefore, the best size of  $TiO_2$  grating height is  $0.7 \,\mu m$  and this height is employed in the following sections.

**Incident angle dependence and polarization-sensitivity.** The omnidirectional characteristics of the micro-structured perovskite solar cell are illustrated by the optical absorption for various incident angle varying from 0° to 60° by the step of 15°, as shown in Fig. 6. Since the polarization of the incident wave strongly influences the spectral features of the structured surface at oblique incidence, both the s- and p-polarizations are considered. Figure 6a shows the absorption of the structured surface at different incident angles for s-polarization. Both the overall absorption and intrinsic absorption exhibit perfect omnidirectional spectral features for incident angle ranging from 0° to 60°. The inset in Fig. 6a shows the much clearer and enlarged view of the overall absorption at different incident angles for s-polarization. The overall absorption spectra slightly oscillate around 0.96 and the incident angle has little effect on the high absorption of the structured surface E. The intrinsic absorption at oblique incidence is slightly lower than that at the incident angle of 0°. However, the intrinsic absorption still keeps higher than 0.7 at the wavelength from  $0.4\,\mu m$  to  $0.8\,\mu m$  at oblique incidence, even the incident angle is increased to as large as 60°. This states that the structured surface of perovskite cell possesses the omnidirectional features for s-polarization. Figure 6b depicts the absorption of the structured surface E at different incident angles for p-polarization. The inset in Fig. 6b is the shows the enlarged view of the overall absorption at different incident angles for p-polarization. The effect of incident angle on the overall absorption is negligible and the overall

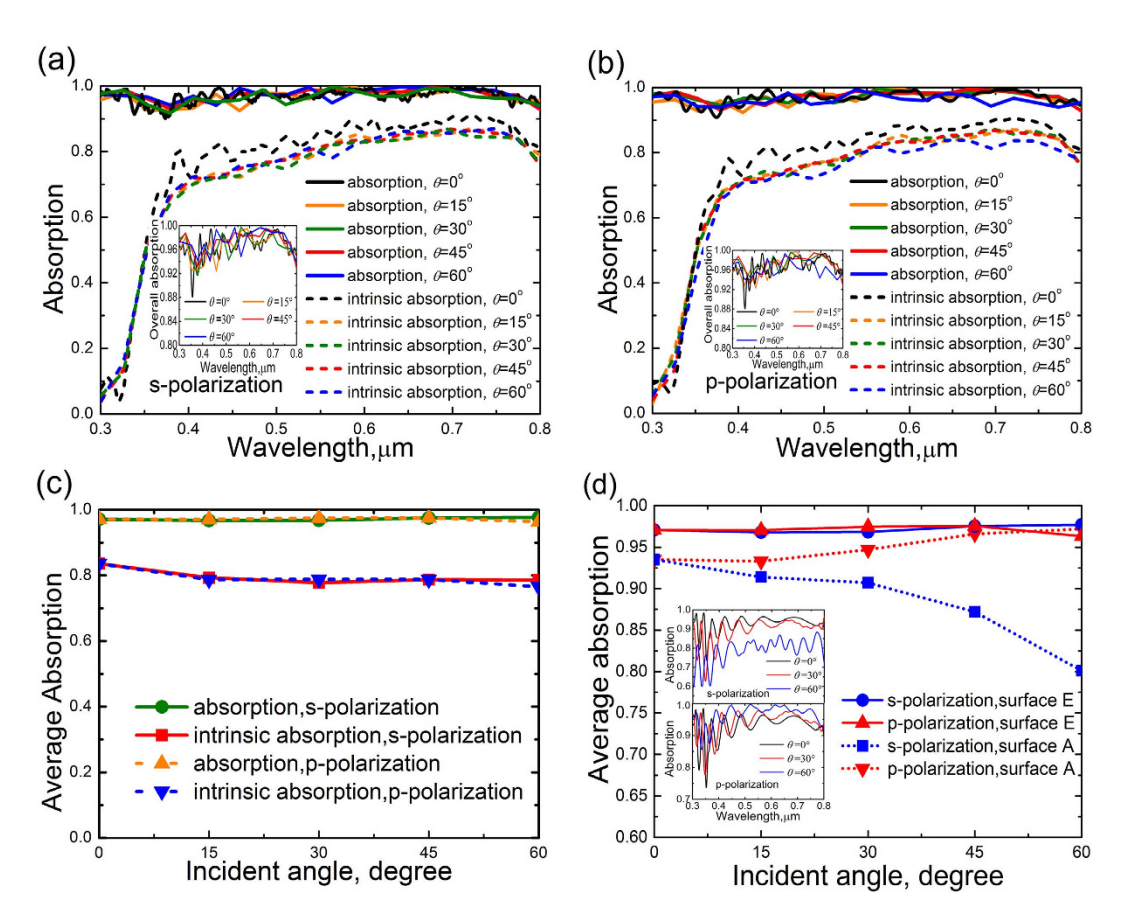


Figure 6. Incident angle-dependence of the spectral absorption for s-polarization and p-polarization of the structured surface E, in which the SiO<sub>2</sub> moeh-eye grating is combined with TiO<sub>2</sub> grating. (a) S-polarization. The inset shows the enlarged view of overall absorption of at different incident angles for s-polarization. (b) P-polarization. The inset shows the enlarged view of overall absorption of at different incident angles for s-polarization. (c) Average absorption for s-polarization and p-polarization. (d) Comparison between the average absorption of structured surface E and structured surface A at different incident angles for s- and p-polarizations. The inset shows the spectral absorption of structured surface A for s- and p-polarizations at different incident angles.

absorption in the wavelength band of 0.3–0.8 µm keeps a high level around 0.96. The intrinsic absorption is slightly reduced with the increase of incident angle while the intrinsic absorption is always above 0.7 at the wavelength from 0.4 µm to 0.8 µm. It is demonstrated that the omnidirectional feature is also realized by the structured surface E for p-polarization. In order to evaluate the overall optical omnidirectional characteristic of the structured surface E, the average overall absorption and the average intrinsic absorption are illustrated in Fig. 6c. The average absorption of the structured surface E for s-polarization almost coincides with that for p-polarization. The structured surface maintains a high overall absorption around 0.97 in the wide incident angle of 0°-60°. The average intrinsic absorption is slightly reduced with the increase of incident angle. However, the reduction is very limited and the intrinsic absorption is maintained at a high level. As the incident angle is increased from 0° to 60°, the average intrinsic absorption is reduced from 0.836 to 0.786 for s-polarization and from 0.836 to 0.766 for p-polarization. The high intrinsic absorption is effectively realized in a wide incident angle range of 0°-60°. In order to highlight the advantage of the structured surface E on light trapping, the average absorption of structured surface E at different incident angles for s- and p-polarizations is compared with that of structured surface A (planar film in Fig. 2a) in Fig. 6d. The inset in Fig. 6d shows the spectral absorption of structured surface A. The absorption of structured surface A is obviously polarization-sensitive and incident angle-dependent. In contrast, the variation of the average absorption of structured surface E for both the s- and p-polarizations is negligible. Simultaneously, the absorption of structured surface E for both the s- and p-polarizations is remarkably larger than that of structured surface A in a wide incident angle range. Therefore, the structured surface E exhibits great superiority of omnidirectional and polarization-insensitive light-trapping compared with the structured surface A.

# Discussion

In conclusion, we have developed a comprehensive design approach for omnidirectional high-performance perovskite solar cell with coupled optical-electrical simulations, in which the selection of structured surface, effect of geometry parameters, incident-angle dependence and polarization-sensitivity are considered. The optical and electrical performances of five different structured surfaces are theoretically investigated. The simulated results are compared to select a best structured sruface for perovskite cell. The results reveal that the CH<sub>3</sub>NH<sub>3</sub>PbI<sub>3</sub> grating can obviously enhance the absorption of  ${\rm CH_3NH_3PbI_3}$  layer to generate more electron-hole pairs while the recombination is greatly increased and the  $J_{\rm sc}$  is greatly reduced for the significant surface recombination velocity. The structured surface with TiO<sub>2</sub> grating and SiO<sub>2</sub> grating is the best structured surface for its high absorption due to the gradient refractive index of SiO<sub>2</sub> grating and double scatterings of TiO<sub>2</sub> grating and SiO<sub>2</sub> grating. Simultaneously, the TiO<sub>2</sub> grating and SiO<sub>2</sub> grating have little effect on the recombination of perovskite cell and the efficiency of the cell is greatly increased. The absorption is enhanced with the increase of SiO<sub>2</sub> grating height due to the reduced gradient of effective refractive index. The TiO<sub>2</sub> grating can effectively enhance the intrinsic absorption of perovskite solar cell due to the scattering of TiO<sub>2</sub> grating and the TiO<sub>2</sub> grating height of 0.7  $\mu$ m shows the best absorption. The power conversion efficiency can be increased to 18.2% with  $J_{\rm sc}=22.98\,{\rm mA/cm^2}$  and  $V_{\rm oc}=0.96\,{\rm V}$ . The structured surface E exhibits excellent omnidirectional high absorption in the wide incident angle range of 0°-60° and the structured surface possesses favorable polarization-insensitive features. As such, the comprehensive design approach investigated in this paper can highlight the better utilizing of the solar energy with perovskite cell.

#### Methods

The evaluation of PV cell performance contains two aspects: one is the optical absorption and the other is carrier transport. The optical absorption can be calculated by FDTD method, which is developed for solving Maxwells' equations that describes the light propagation and interactions with the cell surface<sup>41</sup>

$$\begin{cases}
\nabla \times \mathbf{H} &= \frac{\partial \mathbf{D}}{\partial t} \\
\nabla \times \mathbf{E} &= -\frac{\partial \mathbf{B}}{\partial t} \\
\mathbf{D} &= \varepsilon \mathbf{E} \\
\mathbf{B} &= \mu \mathbf{H}
\end{cases} \tag{1}$$

where **E** is the electric field, **H** is the magnetic field, **D** is the electric displacement field, **B** is the magnetic flux density,  $\varepsilon$  is the complex permittivity, and  $\mu$  is the complex permeability. Since  $\varepsilon$  is frequency-dependent, the frequency domain equation  $\mathbf{D}(\omega) = \varepsilon(\omega) \cdot \mathbf{E}(\omega)$  should be transformed into the time domain by the auxiliary difference equation (ADE). Convergence was assured by using a time step determined by<sup>41</sup>

$$\Delta t = \delta/(2 \cdot c) \tag{2}$$

where  $\delta$  is the smallest spatial increment and c is the speed of light in vacuum. The mesh size significantly influences the convergence and accuracy of the simulation, as reported by Barnes<sup>42</sup>. The mesh size and the time step are respectively set to 2 nm and 0.002 fs to ensure the convergence and accuracy of the calculation at the normal incidence. Since the structured surface is periodic in x- and y- directions, the periodic boundary conditions are applied in x- and y- directions at normal incidence meanwhile Bloch boundary conditions are applied for oblique incidence. The perfectly matched layers (PML) are used in z-direction. FDTD is a mature numerical method which is extensively used in computational electromagnetics. The detailed algorithm of FDTD method has been widely reported and one can find it in many literatures<sup>43</sup>. In order to evaluate the overall optical performance of the perovskite-based solar cells, the average absorption is calculated by<sup>44</sup>

$$A_{\rm av} = \frac{\int_{\lambda} A_{(\lambda)} I_{(\lambda)} d\lambda}{\int_{\lambda} I_{(\lambda)} d\lambda}$$
(3)

where  $A_{(\lambda)}$  is the spectral absorption.  $I_{(\lambda)}$  is for AM 1.5 emissions<sup>45</sup>.

The numerical simulation at large incident angles become difficult on some extent. Oh and Escuti developed an efficient implementation of FDTD method through periodic media with arbitrary anisotropy and the FDTD algorithm is validated against rigorous coupled-wave analysis method at oblique incidence<sup>46</sup>. In order to ensure the accuracy and acceptable convergence of the FDTD simulation at larger oblique incidence, the minimum mesh size of 1 nm, the modified PMLs with 256 layers and the Bloch boundary condition are used in the calculation. The FDTD algorithm in this paper is validated to be reliable at large incident angle by the agreement between the FDTD simulated results of film stack at incident angle of 45° and 60° and the results calculated by the well-known transfer-matrix formalism (Supplementary Fig. S4). The average values of spectral absorption calculated by FDTD and transfer-matrix methods are compared (Supplementary Table S2) to evaluate the overall simulation accuracy. The negligible difference between the average values of absorption calculated by FDTD and transfer-matrix methods proves that simulated results by FDTD can reveal the absorption performance of the structured surface at oblique incidence, even at large incident angles.

By assuming that each photon absorbed by  $\mathrm{CH_3NH_3PbI_3}$  layer can generate an electron-hole pair, the optical generation can be expressed as  $^{47}$ 

$$G_{opt}(r) = \int_{300 \, \text{nm}}^{\lambda_g} \frac{\varepsilon'' \left| E(r, \, \lambda) \right|^2}{2\hbar} I(\lambda) d\lambda \tag{4}$$

where E is the electric field,  $\varepsilon''$  is the imaginary part of the permittivity of the semiconductor material,  $\hbar$  is the reduced Planck constant, and  $\lambda_g$  is the cut-off wavelength corresponding to the band gap of the semiconductor. The carrier transport process can be described by the coupled nonlinear equations of Poisson, continuity, and drift-diffusion equations as  $^{48-50}$ 

$$\nabla \cdot (\varepsilon \nabla \phi) = q(p - n + N_D - N_A) \tag{5}$$

$$\nabla \cdot J_n = -q(G - R) \tag{6}$$

$$\nabla \cdot J_p = q(G - R) \tag{7}$$

$$J_n = -q\mu_n n \nabla \phi + q D_n \nabla n \tag{8}$$

$$J_p = -q\mu_p p \nabla \phi - q D_p \nabla p \tag{9}$$

where q stands for the electron charge,  $\phi$  for the electrical potential, n(p) for the electron (hole) concentration,  $N_D(N_A)$  for the donor (acceptor) doping concentration,  $I_n(J_p)$  for the current density of electron (hole), G for the optical generation rate obtained from optical simulation, R is the carrier recombination rate,  $\mu_n(\mu_p)$  is the electron (hole) mobility, and  $D_n(D_p)$  is the electron (hole) diffusion coefficient. The Shockley-Read-Hall recombination and surface recombination are involved in the electrical simulation as<sup>48</sup>

$$R_{SRH} = \frac{np - n_i^2}{\tau_p \left(n + n_i \exp\left(\frac{E_t - E_i}{k_B T}\right)\right) + \tau_n \left(p + n_i \exp\left(-\frac{E_t - E_i}{k_B T}\right)\right)}$$
(10)

$$R_{surf} = \frac{np - n_i^2}{\frac{1}{S_p} \left( n + n_i \exp\left(\frac{E_{ls} - E_i}{k_B T}\right) \right) + \frac{1}{S_n} \left( p + n_i \exp\left(-\frac{E_{ls} - E_i}{k_B T}\right) \right)}$$
(11)

where  $\tau_n(\tau_p)$  for the electron (hole) lifetime,  $n_i$  for the intrinsic carrier concentration, and  $S_n(S_p)$  is the surface recombination velocity of electron (hole).  $E_t$  is the defect energy level.  $E_i$  is the Femi energy level.  $E_t$  is the surface defect energy level.  $k_B$  is the Boltzmann constant.

For the semiconductor material, the electron (hole) lifetime is related to effective electron (hole) mass. The effective electron (hole) mass can be expressed as  $^{51}$ 

$$m_n^* = (N_c/2)^{2/3} * h^2/(2\pi k_B T)$$
 (12)

$$m_p^* = (N_v/2)^{2/3} * h^2/(2\pi k_B T)$$
 (13)

where,  $N_c$  and  $N_v$  are respectively the effectively conduction band density and valence band density. h is the Planck constant. T is the cell temperature and  $T = 300 \, \mathrm{K}$  is selected for the electrical simulation. Consequently, the electron (hole) lifetime are  $^{52,53}$ 

$$\tau_{n,p} = \left(\sigma_{n,p} N_t \sqrt{\frac{3k_B T}{m_{n,p}^*}}\right)^{-1} \tag{14}$$

where,  $\sigma_{n,p}$  is the capture cross-section.  $N_t$  is the defect density.

In a semiconductor or conductor, the work function describes the energy cost of removing an electron from the intrinsic energy level and placing is at infinity. This property directly influences the charge output. The work-function of the semiconductor can be expressed as  $^{54}$ 

$$\phi = \chi + \frac{E_g}{2} + \frac{k_B T}{2} \ln \frac{N_c}{N_v}$$
 (15)

where  $\chi$  is the electron affinity and  $E_g$  is the band gap energy.

#### References

- 1. Cheng, Y. J., Yang, S. H. & Hsu Synthesis of conjugated polymers for organic solar cell applications. Chem. Rev. 109, 5868-5923 (2009).
- 2. Adachi, M. M., Anantram, M. P. & Karim, K. S. Core-shell silicon nanowire solar cells. Sci. Rep. 3, 1-6 (2013).
- 3. Liu, Y. et al. Solution-processed small-molecule solar cells: breaking the 10% power conversion efficiency. Sci. Rep. 3, 1–8 (2013).
- Holman, Z. C. et al. Parasitic absorption in the rear reflector of a silicon solar cell: simulation and measurement of a sub-bandgap reflectance for common dielectric/emtal reflectors. Sol. Energ. Mat. Sol. C. 120, 426–430 (2014).
- Makableh, Y. F. et al. Enhancement of GaAs solar cell performance by using a ZnO sol-gel anti-reflection coating. Sol. Energ. Mat. Sol. C. 123, 178–182 (2014).
- 6. Ren, Z. et al. Thermal assisted oxygen annealing for high efficiency planar CH3NH3PbI3 perovskite solar cell. Sci. Rep. 4, 6752 (2014).
- 7. Noel, N. K. et al. Lead-free organic-inorganic tin halide perovskite for photovoltaic applications. Energy Environ. Sci. 7, 0.61-3068 (2014)
- 8. Tress, W. et al. Understanding the rate-dependent J-V hysteresis, slow time component, and aging in CH3NH3PbI3 perovskite solar cells: the role of a compensated electric field. Energy Environ. Sci. 8, 995–1004 (2015).
- 9. Wang, K. C. et al. P-type mesoscopic nickel oxide/organometallic perovskite heterojunction solar cells. Sci. Rep. 4, 4756 (2014).

- 10. Brivio, F., Walker, A. B. & Walsh, A. Structural and electronic properties of hybrid perovskite for high-efficiency thin-film photovoltaics from first-principles. *Apl. Mater.* 1, 042111 (2013).
- 11. Baikie, T. et al. Synthesis and crystal chemistry of the hybrid perovskite (CH<sub>3</sub>NH<sub>3</sub>)PbI<sub>3</sub> for solid-state sensitized solar cell applications. J. Mater. Chem. A 1, 5628 (2013).
- 12. Okamoto, Y. & Suzuki, Y. Perovskite-type SrTiO3, CaTiO3 and BaTiO3 porous film electrodes for dye-sensitized solar cells. J. Ceram. Soc. Jpn. 122, 728–731 (2014).
- Eperon, G. E., Burlakov, V. M., Docampo, P., Goriely, A. & Snaith, H. J. Morphological control for high performance, solution-processed planar heterojunction perovskite solar cells. Adv. Funct. Mater. 24, 151–157 (2014).
- 14. Umari, P., Mosconi, E. & Angelis, F. D. Relativistic GW calculations on CH<sub>3</sub>NH<sub>3</sub>PbI<sub>3</sub> and CH<sub>3</sub>NH<sub>3</sub>SnI<sub>3</sub> perovskite for solar cell applications. *Sci. Rep.* 4, 4467 (2014).
- 15. Snaith, H. J. et al. Efficiency enhancements in solid-state hybrid solar cells via reduced charge recombination and increased light capture. Nano Lett. 7, 3372–3376 (2007).
- 16. Bach, U. et al. Solid-state dye-sensitized mesoporous TiO2 solar cells with high photon-to-electron conversion efficiencies. *Nature* 395, 583–585 (1998).
- Kim, H. S. et al. Lead lodide perovskite sensitized all-solid-state submicron thin film mesoscopic solar cell with efficiency exceeding 9%. Sci. Rep. 2, 1–7 (2012).
- 18. Lee, M. M., Teuscher, J., Miyasaka, T., Murakami, T. N. & Snaith, H. J. Efficient hybrid solar cells based on meso-superstructured organometal halide perovskites. *Science* 338, 643–647 (2012).
- Kim, H. S. et al. High efficiency solid-state sensitized solar cell-based on submicrometer butile TiO<sub>2</sub> nanorod and CH<sub>3</sub>NH<sub>3</sub>PbI<sub>3</sub> perovskite sensitizer. Nano Lett. 13, 2412–2417 (2013).
- 20. Stranks, S. D. *et al.* Electron-hole diffusion lengths exceeding 1 micrometer in an organometal trihalide perovskite absorber. *Science* **342**, 341–344 (2013).
- 21. Ball, J. M., Lee, M. M., Hey, A. & Snaith, H. J. Low-temperature processed meso-superstructured to thin-film perovskite solar cells. *Energy Environ. Sci.* 6, 1739–1743 (2013).
- Liu, M., Johnston, M. B. & Snaith, H. J. Efficient planar heterojunction perovskite solar cells by vapour deposition. *Nature* 501, 395–398 (2013).
- 23. Snaith, H. J. Perovskite: the emergence of a new era for low-cost, high-efficiency solar cells. J. Phys. Chem. Lett. 4, 3623-3630 (2013).
- 24. Liu, D. & Kelly, T. L. Perovskite solar cells with a planar heterojunction structure prepared using room-temperature solution processing techniques. *Nature Photon.* 8, 133–138 (2014).
- 25. Zhou, H. et al. Interface engineering of highly efficient perovskite solar cells. Science 345, 542-546 (2014).
- NREL, Best research-cell efficiencies. (2015) Available at: http://www.nrel.gov/ncpv/images/efficiency\_chart.jpg. (Accessed: 18th November 2015).
- 27. Liu, F. et al. Numerical simulation: toward the design of the high-efficiency planar perovskite solar cells. Appl. Phys. Lett. 104, 253508 (2014).
- 28. Ball, J. M. *et al.* Optical properties and limiting photocurrent of thin-film perovskite solar cells. *Energy Environ. Sci.* **8,** 602–609 (2015).
- 29. Spinelli, P., Verschuuren, M. A. & Polman, A. Broadband omnidirectional antireflection coating based on subwavelength surface Mie resonators. *Nat. Commun.* 3, 1–5 (2012).
- 30. Song, Y. M., Jang, S. J., Yu, J. S. & Lee, Y. T. Bioinspired parabola subwavelength structures for improved broadband antireflection. Small 6, 984–987 (2010).
- 31. Tommila, A. et al. Moth-eye antireflection coating fabricated by nanoimprint lighography on 1 eV dilute nitride solar cell. Prog. Photovolt. Res. Appl. 21, 1158–1162 (2013).
- 32. Yamada, N., Ijiro, T., Okamoto, E., Hayashi, K. & Masuda, H. Characterization of antireflection moth-eye film on crystalline silicon photovoltaic module. *Opt. Express* 19, A118–A125 (2011).
- 33. Han, L. et al. GaN microdomes for broadband omnidirectional antireflection for concentrator photovoltaics. *In SPIE OPTO* 862016 (International Society for Optics and Photonics, 2013).
- 34. Ball, J. M. Supplementary information for "optical properties and limiting photocurrent of thin-film perovskite solar cells". *Energy Environ. Sci.* 8 (2015).
- 35. Palik, E. D. Handbook of Optical Constants of Solids (Academic press, New York, 1985).
- Raut, H. K., Ganesh, V. A., Nair, A. S. & Ramakrishna, S. Anti-reflective coatings: a critical, in-depth review. *Energy Environ. Sci.* 4, 3779–3804 (2011).
- 37. Balenzategui, J. L. & Chenlo, F. Measurement and analysis of angular response of bare and encapsulated silicon solar cells. *Sol. Energ. Mat. Sol. C.* **86**, 53–83 (2005).
- 38. Wang, F. et al. Development of nanopatterned fluorine-doped tin oxide electrodes for dye-sensitized solar cells with improved light trapping. Appl. Mater. Interfaces 4, 1565–1572 (2012).
- 39. Lee, J., Park, J. & Lee, M. Nanostructured TiO2 diffraction grating fabricated via imprinting and TiCl<sub>4</sub> treatment. *J. Mater. Chem. C* 2, 981–985 (2014).
- 40. Park, K. T. *et al.* Lossless hybridization between photovoltaic and thermoelectric devices. *Sci. Rep.* **3**, 1–6 (2013).
- 41. Yang, L. L., Xuan, Y. M., Han, Y. G. & Tan, J. J. Investigation on the performance enhancement of silicon solar cells with an assembly grating structure. *Energy Convers. Manage* **54**, 30–37 (2012).
- 42. Barnes, W. L. Comparing experiment and theory in plasmonics. J. Opt. A: Pure Appl. Opt. 11, 114002 (2009).
- 43. Ge, D. & Yan, Y. Finite-Difference Time-Domain Method for Electromagnetic Waves (Publishing house of Xidian University, Xi'an, 2011).
- Meng, X. et al. Combined front and back diffraction gratings for broad band light trapping in thin film solar cell. Opt. Express 20, A560–A571 (2012).
- 45. Website for NREL's AM1.5 Standard Dataset. Reference solar spectral irradiance: air mass 1.5. (2015). Available at: http://rredc.nrel.gov/solar/spectra/am1.5. (Accessed: 18th November 2015).
- 46. Oh, C. & Escuti, M. J. Time-domain analysis of periodic anisotropic media at oblique incidence: an efficient FDTD implementation. *Opt. Express* 14, 11870–11884 (2006).
- 47. Da, Y. & Xuan, Y. M. Role of surface recombination in affecting the efficiency of nanostrucutred thin-film solar cells. *Opt. Express* 21, A1065–A1077 (2013).
- 48. Selberherr, S. Analysis and Simulation of Semiconductor Device (Springer Science & Business Media, New York, 2012).
- 49. Sha, W. E., Choy, W. C., Wu, Y. & Chew, W. C. Optical and electrical study of organic solar cells with a 2D grating anode. *Opt. Express* 20, 2572–2580 (2012).
- 50. Li, X. et al. Multi-dimensional modeling of solar cells with electromagnetic and carrier transport calculations. Prog. Photovolt. Res. Appl. 21, 109–120 (2013).
- 51. Zhao, Y. Q., Yao, S. Y. & Shi, Z. F. Semiconductor physics and devices basic principles (Publishing house of electronics industry, Beijing, 2013).
- 52. Schroder, D. K. Carrier lifetimes in Silicon. IEEE Transactions on Electron Devices 44, 160-170 (1997)
- 53. Henry, C. H. & Lang, D. V. Nonradiative capture and recombination by multiphonon emission in GaAs and GaP. *Phys. Rev. B* 15, 989–1016 (1977).
- 54. Anderson, B. L. & Anderson, R. L. Fundamentals of Semiconductor Devices (McGraw-Hill, Inc. New York, 2004).

#### **Acknowledgements**

The authors thank the National Natural Science Foundation of China (Grant no. 51336003) and (Grant no. 50590901) for the supports.

# **Author Contributions**

Y.Z. and Y.X. jointly finished the conceiving of the idea, performing of the simulation and preparation of the manuscript.

# **Additional Information**

**Supplementary information** accompanies this paper at http://www.nature.com/srep

**Competing financial interests:** The authors declare no competing financial interests.

How to cite this article: Zhang, Y. and Xuan, Y. Comprehensive design of omnidirectional high-performance perovskite solar cells. *Sci. Rep.* **6**, 29705; doi: 10.1038/srep29705 (2016).

This work is licensed under a Creative Commons Attribution 4.0 International License. The images or other third party material in this article are included in the article's Creative Commons license, unless indicated otherwise in the credit line; if the material is not included under the Creative Commons license, users will need to obtain permission from the license holder to reproduce the material. To view a copy of this license, visit http://creativecommons.org/licenses/by/4.0/